doi:10.26443/seismica.v5i1.1676

Spatiotemporal Dynamics of Clusters in the Bridge Zone Linking L'Aquila 2009 and Central Italy 2016 Seismic Sequences

Alessandro Vuan * [1,2], **Lauro Chiaraluce** [2,1], **Saeed Yahya Mohanna** [3], **Monica Sugan** [1]

[1]Department of Seismological Research, National Institute of Oceanography and Applied Geophysics - OGS, Trieste, Italy , [2]National Earthquake Observatory, National Institute of Geophysics and Volcanology - INGV, Rome, Italy , [3]Department of Earth, Planetary, and Space Sciences, University of California Los Angeles - Los Angeles, CA, USA

Author contributions: *Conceptualization*: Alessandro Vuan, Lauro Chiaraluce. *Methodology*: Alessandro Vuan, Lauro Chiaraluce, Monica Sugan, Saeed Yahya Mohanna. *Software*: Alessandro Vuan, Saeed Yahya Mohanna. *Validation*: Alessandro Vuan, Lauro Chiaraluce, Monica Sugan, Saeed Yahya Mohanna. *Formal Analysis*: Alessandro Vuan. *Investigation*: Alessandro Vuan, Lauro Chiaraluce, Monica Sugan. *Writing - Original draft*: Alessandro Vuan. *Writing - Review & Editing*: Alessandro Vuan, Lauro Chiaraluce, Monica Sugan, Saeed Yahya Mohanna. *Visualization*: Alessandro Vuan. *Supervision*: Alessandro Vuan. *Funding acquisition*: Alessandro Vuan.

Abstract We analyze the spatiotemporal evolution of earthquake clusters in the Campotosto area, located between the L'Aquila 2009 and Central Italy 2016 seismic sequences. This region has experienced several moderate earthquakes (M_W 5–5.5) and persistent low-level seismicity. Using a hierarchical density-based algorithm on high-resolution catalogs, we identify clusters lasting from days to months and migrating at rates of meters to kilometers per day. These clusters alternate between phases of rapid expansion and slower diffusion, reflecting complex interactions among fluids, aseismic slip, and seismic rupture across fault segments. Energy release within clusters is low, with effective stress drop ranging from 0.01 to 1 MPa, suggesting diverse driving processes. Clusters with larger spatial extents tend to exhibit lower effective stress drop, implying a significant aseismic slip component, consistent with remote sensing observations. Our findings indicate that deep fluids promote multiphase slip and fault reactivation, influencing seismicity across fault segments with varying criticality. Variations in fault orientation and dip further contribute to heterogeneous slip distribution, affecting both energy release and cluster formation.

Production Editor: Yen Joe Tan
Handling Editor: Giuseppe Petrillo
Copy & Layout Editor: Théa Ragon

Received: September 22, 2025
Accepted: January 24, 2026
Published: February 9, 2026

Non-technical summary The activation of faults by nearby earthquakes can occur through various mechanisms, each influenced by the state of stress and its sudden fluctuations, fault geometry, frictional properties and external forces. The basic types of fault activation include dynamic triggering, earthquake interaction, changes in pore water pressure, and aseismic transients. These processes often occur almost simultaneously, making it challenging to identify the driving mechanism responsible for changes in crustal volumes. Limited knowledge of fault geometries, their segmentation, and other structural heterogeneities hinders further investigation of complex and productive earthquake sequences. Here, we analyze the behavior of the Campotosto bridge area and its activation following the main earthquakes in central Italy. The area experienced three earthquakes with 5<M_W<5.5 immediately after the L'Aquila M_W 6.3 earthquake and four similar events two and a half months after the Norcia M_W 6.5 earthquake. We use high-resolution earthquake catalogs to identify clusters that stand out from the background seismicity suggesting mechanisms that may have influenced the frictional resistance of the faults and the role of fluids in reducing the effective normal stress, thereby facilitating fault slip.

1 Introduction

In the last 20 years, Central Italy has experienced two significant seismic sequences: the M_W 6.3 L'Aquila earthquake in 2009 and the M_W 6.5 Central Italy earthquake in 2016. The two main sequences converge in the so-called Campotosto seismic zone (CSZ in Fig. 1), an area where several fault segments were activated by a series of moderate magnitude earthquakes (M_W<5.5) in 2009 and 2017 (e.g., Chiaraluce et al., 2017; Falcucci et al., 2018). The CSZ was hit by three earthquakes with 5<M_W<5.5 immediately after the L'Aquila M_W 6.3 event, and four similar events two and a half months after the Norcia M_W 6.5 earthquake. All these earthquakes exhibited a northwest-trending rupture directivity (e.g., Calderoni et al., 2017) and an average strike, dip and rake of 320°, 57° and -90°, respectively (e.g., Brennan Brunsvik et al., 2021; Artale Harris et al., 2022; Locchi et al., 2024). Thus, the CSZ comprises a complex system of fault segments 5-15 km long within a 450 km^2 area (Fig. 1).

High-resolution earthquake catalogs covering both the period before and after the main events are available (e.g., Valoroso et al., 2013; Sugan et al., 2014; Tan et al., 2021; Vuan et al., 2017; Sugan et al., 2023; Waldhauser

*Corresponding author: avuan@ogs.it

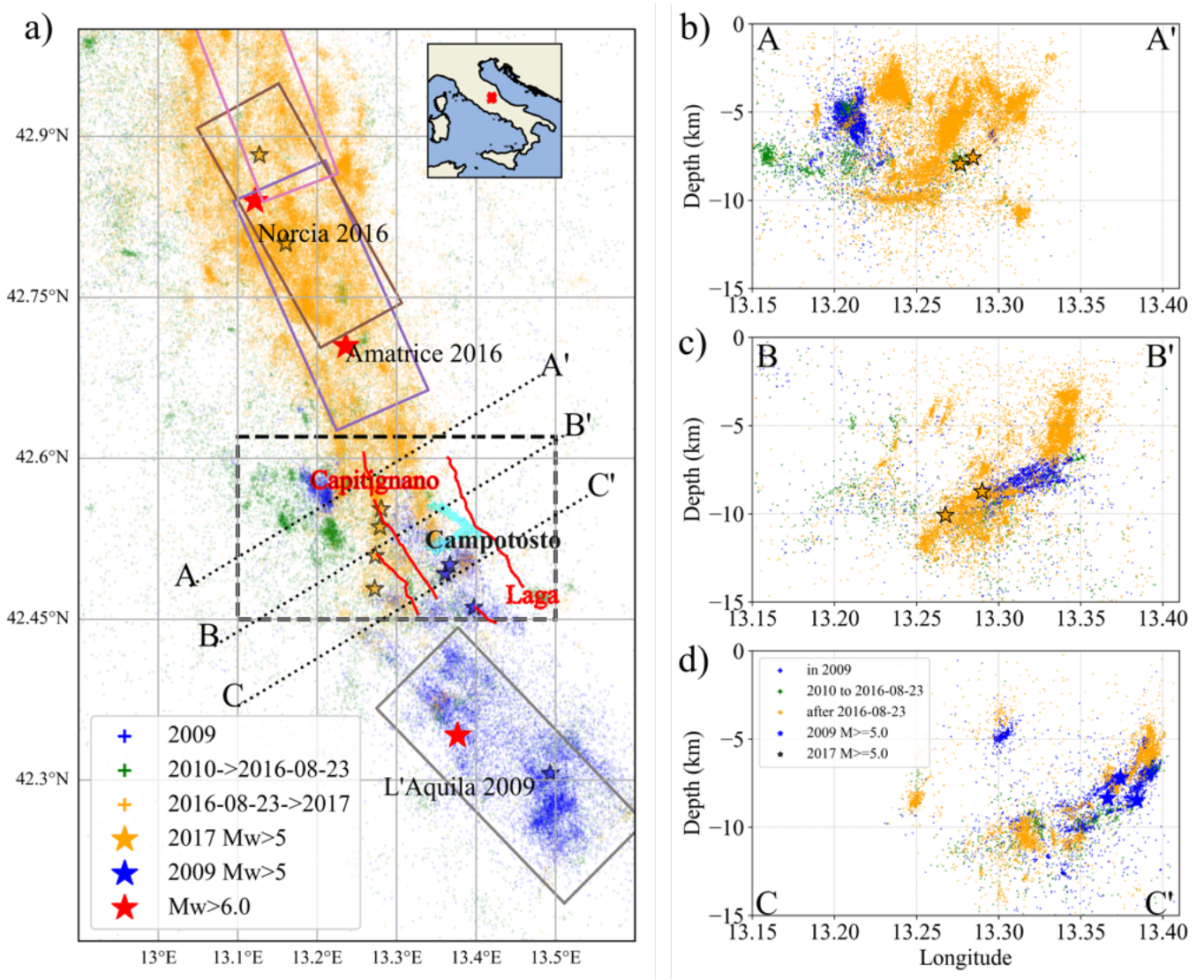

Figure 1 a) Overview map of seismic activity in central Italy since 2009, based on seismic catalogs from Valoroso et al. (2013); Sugan et al. (2023), and Waldhauser et al. (2021). The 2009 L'Aquila seismic sequence in the southeastern sector is shown in blue, while the 2016–2017 sequence is shown in orange. Green dots represent seismicity during the interseismic period (2010 to the onset of the 2016 sequence). Colored rectangles indicate the surface projections of the main finite fault solutions (Cirella et al., 2009; Tinti et al., 2016; Chiaraluce et al., 2017). The black dashed rectangle outlines the Campotosto Seismic Zone (CSZ). Red curved lines within the CSZ mark the surface trace of major southwest-dipping normal faults (Faure Walker et al., 2021). b–d) Projected cross-sections along profiles A–A', B–B', and C–C', respectively. Red stars denote earthquakes with $M_W > 6$. The outline of the Campotosto water reservoir is also shown.

et al., 2021; Chiaraluce et al., 2022). These catalogs, compiled using data from dense permanent and temporary networks, have provided detailed spatial distributions of seismic events (e.g., Mancini et al., 2022) and help improve our understanding of fault geometries and segmentation (e.g., Buttinelli et al., 2021; Barchi et al., 2021; Pizzi et al., 2017).

Figure 1 provides a comprehensive overview of seismic activity in central Italy following the 2009 L'Aquila earthquake. The map highlights the spatial distribution of earthquakes from multiple high-resolution catalogs, distinguishing between the 2009 L'Aquila sequence (blue dots), the 2016–2017 Central Italy sequence (orange dots), and the seismicity from 2010 to early 2016 (green dots). Surface projections of the main finite fault models are also shown (Cirella et al., 2009; Tinti et al., 2016; Chiaraluce et al., 2017). Within the CSZ (black dashed area in Fig. 1), red curved lines trace the surface expression of major southwest-dipping normal faults (Faure Walker et al., 2021; Lavecchia et al., 2021). These normal faults are oriented northwest–southeast. Among them, the Laga and Capitignano faults (Fig. 1) play a critical role in the area's seismic dynamics. Both faults, are associated with Quaternary extensional tectonics and exhibit clear geomorphological evidence of recent activity and surface ruptures (e.g., Civico et al., 2016). The CSZ has the potential to generate earthquakes of magnitude up to M_W6.6 and their structural configuration and historical behavior underscore the importance of detailed seismic hazard assessments in this part of the Apennines.

Changes in the P- to S-wave velocity ratio over time, along with low S-wave velocity zones detected by seismic tomography and ambient noise interferometric

Start Date	End Date	Days	M_{max}	N. Events	Catalog	Figure
04/01/2009	12/31/2009	365	5.10	16291	Valoroso et al. (2013)	Fig. 3a, b
01/01/2010	08/23/2016	2424	3.50	30324	Sugan et al. (2023)	Fig. 3c, d
08/24/2016	01/17/2017	146	4.30	18733	Waldhauser et al. (2021)	Fig. 3e, f
01/18/2017	08/31/2017	212	5.40	25853	Waldhauser et al. (2021)	Fig. 3g, h

Table 1 Seismic catalog summary including time intervals, maximum magnitude, number of events, and corresponding figures.

studies (e.g., Soldati et al., 2019; Magnoni et al., 2022), have been linked with the presence of fluids, as well as pore pressure variations in carbonate rocks (e.g., Chiarabba et al., 2018). Moreover, the strongest sequences ruptured fault patches segmented by inherited structural complexities, suggesting dynamic interference during faulting episodes (e.g., De Gori et al., 2023; Piegari et al., 2024).

In the Central Apennines, lithology also plays a fundamental role in controlling fault mechanics and earthquake behavior. Faults hosted in carbonate-bearing rocks exhibit distinct frictional properties, which contribute to heterogeneous stress conditions, in turn affecting the spatial and temporal evolution of seismic sequences such as those of L'Aquila (2009) and Central Italy (2016-2017). Laboratory and field investigations on specific faults further confirm that carbonate-rich faults can host both seismic and aseismic slip, depending on tectonic loading, mineralogy, fault fabric, and fluid pressure (Carpenter et al., 2014; Collettini and Tinti, 2025).

In this study, we focus on the activation and interaction of clustered seismicity within the CSZ, which connects the two sequences and creates a complex setting that poses a significant seismic hazard in the area where the second largest water reservoir in Europe (Fig. 1) is located, bounded by three dams (e.g., Moratto et al., 2023; Tondi et al., 2020). Although several approaches have suggested the influence of fluids and aseismic deformation (e.g., Malagnini et al., 2010, 2012; Cheloni et al., 2019), some important questions about the generation mechanism of the numerous CSZ events with M_W > 5 occurring at different times require further investigation, as does the correlation between the nearby M_W > 6 earthquakes and the geometric complexity of the fault system. We also examine whether the complex geometry of the CSZ contributed to the splitting and reactivation of the slip into different patches over time. To this end, we use high-resolution earthquake catalogs covering the 2009–2017 time window and apply methods that identify and classify the spatio-temporal dynamics of clustered seismicity relative to the background.

In the following, we provide a comprehensive description of the CSZ including an analysis of seismic activity using a hierarchical, density-based clustering method. This advanced technique enables us to effectively separate and identify distinct seismic clusters active in the area. For each cluster, we define its spatial extent, duration, and when possible, the migration pattern of the seismic front. This analysis helps us understand the temporal and spatial evolution of seismic events within each cluster. In addition, for some clusters we calculate the diffusivity values and the effective stress drop, which are essential for evaluating the released energy and prevailing stress conditions. Finally, we interpret our results and discuss how fault geometry, possible source mechanisms and triggering phenomena may have influenced the observed seismicity patterns, with the aim of improving our understanding of earthquake interactions, aseismic slip, and fluid-related processes.

2 Earthquakes catalog and focal mechanisms in CSZ

To analyse seismicity in the CSZ, we selected high-resolution catalogs (Table 1) covering a period of approximately nine years starting in 2009, focused on the region bounded by latitudes 42.45°–42.6° and longitudes 13.1°–13.5°. Seismicity was truncated to exclude events within the coseismic boxes representing the M_W > 6 fault segments (Cirella et al., 2009; Tinti et al., 2016; Chiaraluce et al., 2017) (Fig. 1).

The catalog from Valoroso et al. (2013) was used for the seismic sequence of the 2009 L'Aquila earthquake. It contains about 60,000 events (blue dots in Fig. 1), located using an automatic detection method for the arrival times of P and S waves combined with cross-correlation and the double difference method (Waldhauser and Ellsworth, 2000). The mean location error is approximately 100 meters as derived from a bootstrap analysis. Approximately 16,300 of these events, which occurred in the CSZ in 2009, were included in the analysis.

From the end of the 2009 L'Aquila sequence to the start of the 2016 Central Italy sequence, we used a template matching-based catalog from Sugan et al. (2023) with more than 31,200 earthquakes in the CSZ (green dots in Fig. 1). The templates were relocated in absolute terms with the NonLinLoc code (Lomax et al., 2000). A double difference method was then applied to refine hypocentral locations, considering only the absolute travel times. The resulting locations have a mean horizontal error of less than 400 meters.

From the beginning of the Amatrice-Norcia sequence in 2016 until August 2017, we used the seismic catalog compiled by Waldhauser et al. (2021), available as CAT4 in Chiaraluce et al. (2022). Hypocentral locations were determined using automatically revised absolute arrival times of the P- and S-waves (Spallarossa et al., 2021) combined with relative arrival times from cross-correlation measurements within the HypoDD code (Waldhauser and Ellsworth, 2000). The mean horizon-

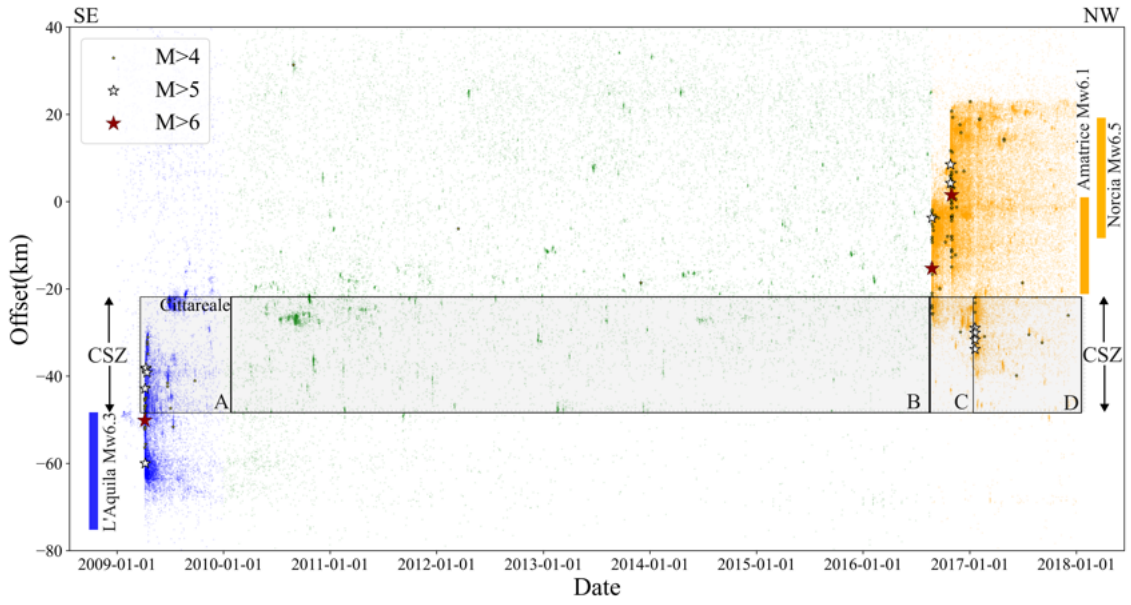

Figure 2 Distribution of earthquakes along the strike, categorized by magnitude. The dots represent events occurring at depths of 0-20 km and the colors distinguish the different catalogs used as shown in Figure 1. The Campotosto Seismic Zone (CSZ) is shaded in gray and includes events with M>5 during phases A and D, following the M>6 earthquakes of 2009 and 2016. Phase B likely represents the background seismicity level, while phase C precedes the reactivation of the CSZ. The light blue and orange vertical segments indicate the extent of the coseismic ruptures of the main events outside the CSZ.

tal and vertical errors are less than 100 m. Of the nearly 400,000 events in this catalog, we selected the 45,000 that occurred in the CSZ for our analysis (orange dots in Fig. 1).

When the three catalogs are combined, the total number of events in the CSZ exceeds 90,000. Figure S1 shows the frequency magnitude distribution for the three catalogs. The maximum curvature completeness magnitude changes over the 9 years from 0.7 (Valoroso et al., 2013), and 0.4 (Sugan et al., 2023) to 0 (Waldhauser et al., 2021).

Figure S2 shows a zoomed map of seismicity in the study area along with the strike parameters of the focal solutions reported by Artale Harris et al. (2022), Brennan Brunsvik et al. (2021) and Locchi et al. (2024). Locchi et al. (2024) computed moment tensor solutions for the 134 events within the CSZ with magnitudes greater than 3 and evaluated their normalized slip tendency. The centroids of focal solutions for events with M>5 fall within a narrow depth range of 7-9 km. Strike angles range from 312° to 332°, and dip from 38° to 71°. The strike parameters of the M>3 events in 2009, compared to those in 2017, indicate a plane rotation from SE-NW to S-N (Fig. S2c).

3 Spatiotemporal analysis of the CSZ seismicity

The distribution of earthquakes along the fault system strike versus time, categorized by magnitude, is shown in Figure 2.

The Campotosto Seismic Zone (CSZ), shaded in grey in Figure 2, includes events with M>5 during phases A and D following the M>6 events of 2009 and 2016. Phase B likely represents a period of low-level seismicity, while phase C precedes the reactivation of the CSZ in 2017.

In Figure 3, we project the CSZ events for the four phases (as shown in Figure 2 and Table 1) onto space-time diagrams. We adopt a N310° strike, which is closest to the orientation of the main faults along the Apennines.

The temporal evolution of events at depth is projected to emphasize their density within the volume. Space-time diagrams show that seismicity was strongly clustered immediately after the 2009 L'Aquila earthquake (Fig. 3a) and migrated rapidly to the northwest (Movie M1 in the supplement). Figure 3 also provides first-order evidence of seismic front migration and clustering. This clustering suggests an immediate response of the Laga fault system (Fig. 3a) to the L'Aquila mainshock, with seismic activity propagating northwestward. A few months later, the Cittareale sequence was activated (Fig. 2), characterized by a typical pressure-driven slow diffusive pattern (Fig. 3a). For the period between the two major sequences (Fig. 3b), there were no significant changes in seismicity rate from 2010 until 24 August, 2016. In 2016, following the first $M_W > 6$ near Amatrice, we observe a marked increase in seismic activity in the northernmost sector (Fig. 3c). Although the magnitudes and the distances from the study area are similar, the southeastward extension of the events in 2016 is spatially much more limited compared to 2009. Two months later, the main Norcia earthquake (M_W 6.5) marked a peak of seismic activity further to the southeast with well-developed clusters near the area of the

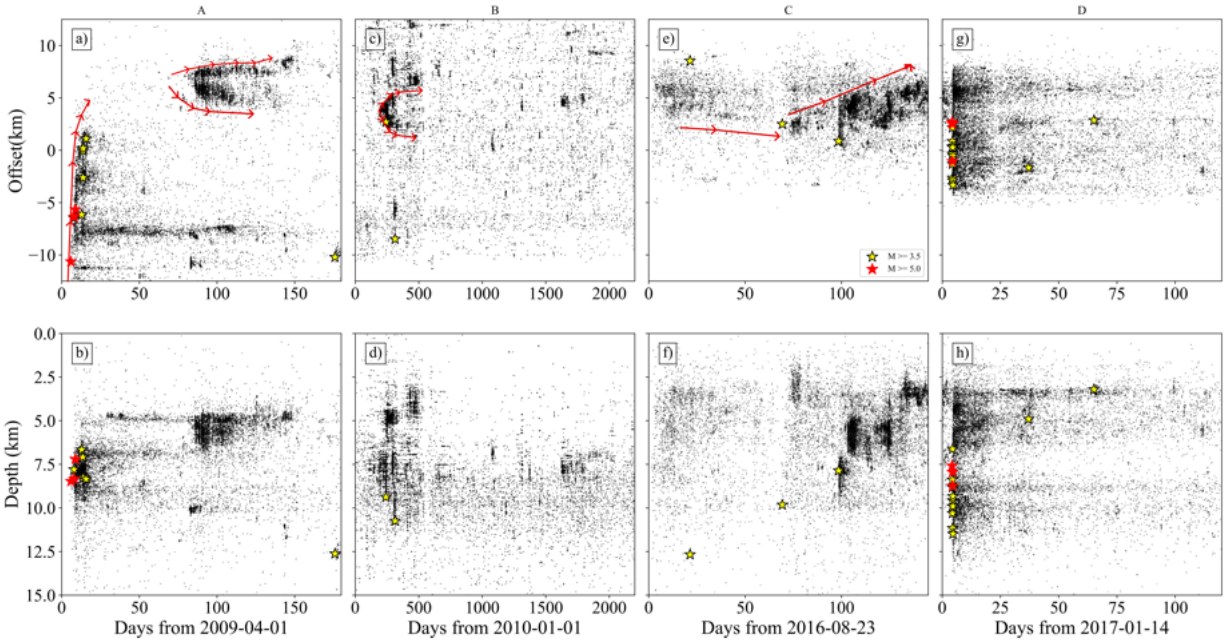

Figure 3 Along-strike (a, c, e, g), and depth (b, d, f, h) projections of seismicity over time for phases A, B, C, and D of Figure 2. The black dots represent events occurring at depths of 0-20 km. The extent of seismicity and migration patterns of clusters are shown in panels a), c) and e) (red arrows). The time interval, the number of events in each phase, and the corresponding catalog are listed in Table 1.

subsequent M_W > 5 events in 2017 (Fig. 3c and Movie M2 in the supplement). This phase culminated in the activation of the entire study area on 18 January 2017, when four M_W > 5 events occurred within a few hours.

The time-depth projections indicate that the hypocenters of events with magnitudes above 5.0 were primarily located at depths between 7 and 9 km (Figs. 3b and 3h). Lower magnitude events in 2009 were generally shallower than those in the 2016-2017 sequence, where many M>3.5 events occurred at depths reaching up to 15 km. We also note that the clustered seismicity preceding the M>5 events in 2017 migrated upward in the northern sector, possibly contributing to fault weakening between 2 and 10 km depth.

We also analyze seismicity rate changes on a grid with 0.3 km increments, expressed as the logarithmic ratio of the number of events 2.5 months before (B) and after (A) change-point dates. Figure S3 shows six time windows indicating significant changes, each characterized by a positive shift (increase) in the ratio within CSZ. From the fluctuations in the seismicity ratio, retrospective analysis reveals that the spatial distribution of seismicity in the CSZ is closely linked to the largest seismic events occurring at its margins.

4 Characteristics of seismicity clusters

We use HDBSCAN (Campello et al., 2013, 2015), a hierarchical density-based algorithm, to identify clusters in the CSZ for the four phases in Table 1. This non-parametric method constructs a cluster hierarchy shaped by the multivariate modes of the underlying distribution. HDBSCAN demonstrates superior sensitivity, up to 82% compared to DBSCAN's (Ester et al., 1996) 50–62% (Hunt and Reffert, 2021), making it the preferred choice. Its ability to handle varying density environments and detect clusters across all density ranges is particularly advantageous for analyzing heterogeneous datasets such as those from the CSZ.

HDBSCAN's parameter setup is generally considered easier and more intuitive than that of DBSCAN, although careful parameter selection remains necessary to balance sensitivity against false positives (Hunt and Reffert, 2021). Unlike methods that search for clusters of a specific shape, HDBSCAN identifies regions of the data that are denser than the surroundings. The goal is to automatically detect and extract clusters of seismicity from an earthquake catalog, using only hypocentral coordinates and time. These clusters represent spatially and temporally constrained periods of increased seismicity rates, potentially driven by processes such as earthquake interaction and triggering, aseismic deformation, fluid migration or a combination of these. Variability in seismicity organization reflects differences in density across space and time; hence the four-dimensional approach. Normalization is required to assign equal weight to spatial and temporal dimensions when considered together.

Density-based clustering identifies populated regions in feature space and can detect outliers, which helps distinguish background seismicity (e.g., Ester et al., 1996; Schoenball and Ellsworth, 2017; Essing and Poli, 2024). In contrast, hierarchical clustering builds a hierarchy based on distances between data points and does not re-

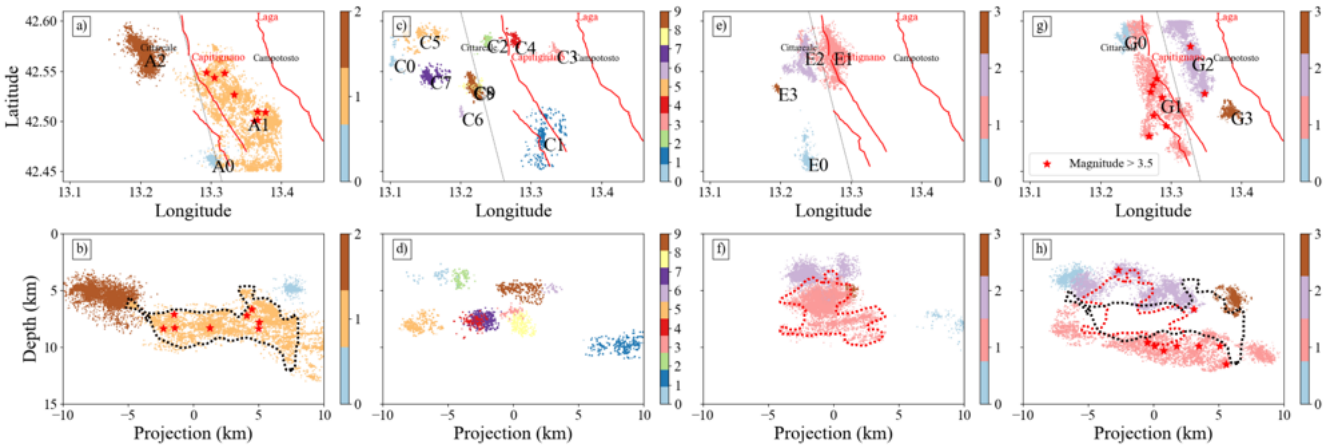

Figure 4 HDBSCAN clusters for the different phases listed in Table 1. The upper panels display the clusters identified on the map, while the lower panels show depth cross-sections of the clusters projected along the average strike (gray line). The projection also shows that cluster A1 (post-L'Aquila 2009) and cluster E1 occupy an intermediate section of the fault system at depth, whereas the reactivation of the system in 2017 generates clusters across a broader area, both at depth and in the shallow portion.

quire a predetermined number of clusters (e.g., Ward, 1963). HDBSCAN transforms the original feature space into a mutual reachability space and adjusts distances based on local densities (Lelis and Sander, 2009). We also use the silhouette score (Rousseeuw, 1987) to optimize the number of clusters by calculating it for a variable minimum number of events within each cluster (from 200 to 800 in steps of 20 events). Figure S4 shows the relationship between minimum cluster size, silhouette score and the number of clusters for the time periods listed in Table 1. Further details on the choice between HDBSCAN and DBSCAN methods, as well as the silhouette score are provided in the supplementary material.

Figure 4 presents the results of the HDBSCAN analysis in both map view and depth cross-section for each phase, with background seismicity filtered out (Fig. S5). The cross sections are projected along strike and reveal clusters of varying spatial extent and duration, ranging from days to months, highlighting key features of the fault system. Following the 2009 L'Aquila earthquake (M_W 6.3), the Laga fault was rapidly activated, with one of the larger clusters (A1) extending northwestward (Figs. 4a, b). Two months later, the shallower Cittareale sequence was triggered (A2 - Figs. 4a, b).

From 2010 until shortly before the M_W 6.1 Amatrice event, clustering was mainly restricted to the northwestern sector, with clusters (C0 – C9) spatially limited and sparsely distributed across the region (Figs. 4c, d).

The M_W 6.5 earthquake, which nucleated near Norcia on 30 October 2016, approximately 50 km away, activated clusters that were more developed in both volume and duration (Figs. 4e, f). A notable cluster (E1 in Fig. 4f) is located north of two M>5 hypocenters of 18 January 2017. Most clusters in 2017 (Figs. 4g, h) filled the volume left untouched by the 2009 sequence, with seismicity at approximately 8-12 km depth (G1 in Fig. 4h) propagating rapidly from northwest to southeast. A second cluster (G2), which also spread rapidly from northwest to southeast and was synchronous with G1, was located at a shallower depth. In the cross-section of Figure 4h, a gap in seismicity is visible between G2 and G1, corresponding to the locations of cluster A1 in 2009 (Fig. 4a) and cluster E1 in 2016 (Fig. 4e).

4.1 Clustering properties and orientation

The redistribution of stress by seismic or aseismic slip can activate and interact with nearby fault segments, promoting the development of clusters (e.g., Hainzl, 2004; Fischer and Hainzl, 2021). When a fault slips, stresses on neighboring faults change, potentially triggering a cascade of seismic events. This interaction can generate complex seismicity patterns. By analyzing cluster properties in Figure 4, such as magnitude distribution over time, orientation, and migration velocity, we aim to gain insight into fault system behavior. We also examine additional cluster properties including duration, size, and seismic front migration velocity. The properties of the clusters shown in Figure 4 are summarized in Table 2. Their duration ranges from 10 days to more than 200 days, while the minimum magnitude averages around 0.5.

A first order classification of seismic clusters follows the methodology proposed by Zhang and Shearer (2016). To quantify the magnitude behavior within these clusters, we use two key metrics: the timing of the largest event (t_m) normalized by the mean time, and the skewness value ($\mu 3$). The skewness of moment release for a given sequence is calculated as in Roland and McGuire (2009) and we also use the normalized time t_m as in Zhang and Shearer (2016). The time of each event (t_i) within the cluster is normalized as (t_i - t_{min})/(t_{max} - t_{min}). Then we calculate t_m as the ratio between the time of the largest moment magnitude event and the mean of the normalized times. If there is more than one event with the maximum magnitude, the first occurrence is chosen.

Figure 5 illustrates the classification framework, which separates fields such as mainshock-aftershock

Cluster	Start Time	Duration (days)	min. mag	Average Depth (km)	N. Events
A1	04/06/2009	190	0.86	8.20	6493
A2	04/17/2009	234	0.64	5.47	5431
A0	04/25/2009	120	0.54	4.85	1105
C8	07/05/2010	76	0.53	7.80	1615
C9	07/13/2010	135	0.43	4.92	3416
C6	09/07/2010	59	0.32	4.86	226
C7	09/30/2010	75	0.41	7.49	2550
C1	11/03/2010	32	0.47	9.79	1411
C0	02/07/2011	80	0.50	3.67	267
C2	02/14/2011	96	0.37	4.06	1535
C3	12/11/2012	14	0.61	6.89	417
C4	06/04/2014	62	0.50	7.78	621
C5	02/05/2016	11	0.55	8.36	489
E1	10/31/2016	77	0.47	6.20	6773
E2	11/01/2016	76	0.49	3.54	3174
E0	11/04/2016	73	0.72	8.23	549
E3	11/30/2016	20	0.47	5.07	132
G1	01/18/2017	203	0.74	9.91	4132
G0	01/18/2017	206	0.35	3.76	917
G2	01/18/2017	216	0.50	4.69	6429
G3	01/18/2017	172	0.50	5.82	990

Table 2 Seismic cluster parameters including start time, duration, min. mag = cluster minimum magnitude, average depth, and number of events.

(M-A) sequences from swarm-like patterns. In addition, mixed clusters, including different types of foreshock (F-M) sequences as described by Peng and Lei (2025), are also classified. This framework enables a first-order analysis of clusters: most exhibit an almost symmetric distribution of magnitudes over time (skewness close to 0) and variable timing of the main event, with only a few clusters falling within the M-A category.

To investigate the principal orientation of each cluster in the volume, we apply Principal Component Analysis (PCA) to the smallest convex set enclosing all points forming a convex polyhedron in 3D (Bradford Barber et al., 1996). The seismicity clouds enclosed by convex polyhedra in Figure 6a are fitted using PCA, providing a 3D variance of the orientation and flatness of the clustered events (Fig. 6b, and Fig. S6 as an example). Table S2 in the supplementary material shows that PCA variance within each cluster is largely confined to a two-dimensional plane. On average the Euclidean distances of the events to the best-PCA plane range from 70 to 490 m. Variations in the azimuthal orientation of these planes across different seismic clusters provide insights into possible segmentation of the fault system, which can be compared with the orientation of the main faults. Movie M3 in the supplement offers additional clues about the 3D position of these planes, which often coincide with the strike of the focal solutions shown in Figure S2. Clusters listed in Table 2, where the number of events is larger, show polyhedra that are generally compressed in 3D and display a nearly planar geometry. Approximating clusters as planes also enables calculation of their areal extent, which, combined with the cumulative seismic moment, is used to infer the effective stress drop.

4.2 Migration velocity of clusters

We evaluate the seismic front velocity of the clusters to better understand the mechanisms driving the spatiotemporal evolution of seismicity in the affected volume. The velocity is computed by projecting the events onto the plane defined for each cluster. We then use the time and location of the first event in each cluster as a reference to compute the absolute radial distance and time difference for subsequent events. Some clusters display ambiguous behavior with multiple phases, alternating between mainshock–aftershock sequences and swarm-like patterns. For these clusters, determining the velocity of the seismic front is challenging. The complex distribution of events hampers a reliable time-distance linear fit suggesting that earthquake interaction may be less organized and that multiple processes could control seismicity patterns.

Figure 7 illustrates the temporal and radial distance distribution of events from the first shock for four selected clusters. Cluster A1, which immediately follows the M_W 6.3 L'Aquila mainshock, is shown in Figure 7a. Initially, seismicity propagates south to north at a migration velocity of approximately 1 km/day, then accelerates to about 3.5 km/day two days after onset. In the following days, the migration velocity decreases and stabilizes at values lower than the initial rate.

In contrast, cluster A2 (Cittareale sequence, Fig. 7b) shows a distinctly different behavior. Here, the apparent migration speed is relatively low (∼0.17 km/day), and despite the high number of low-magnitude events,

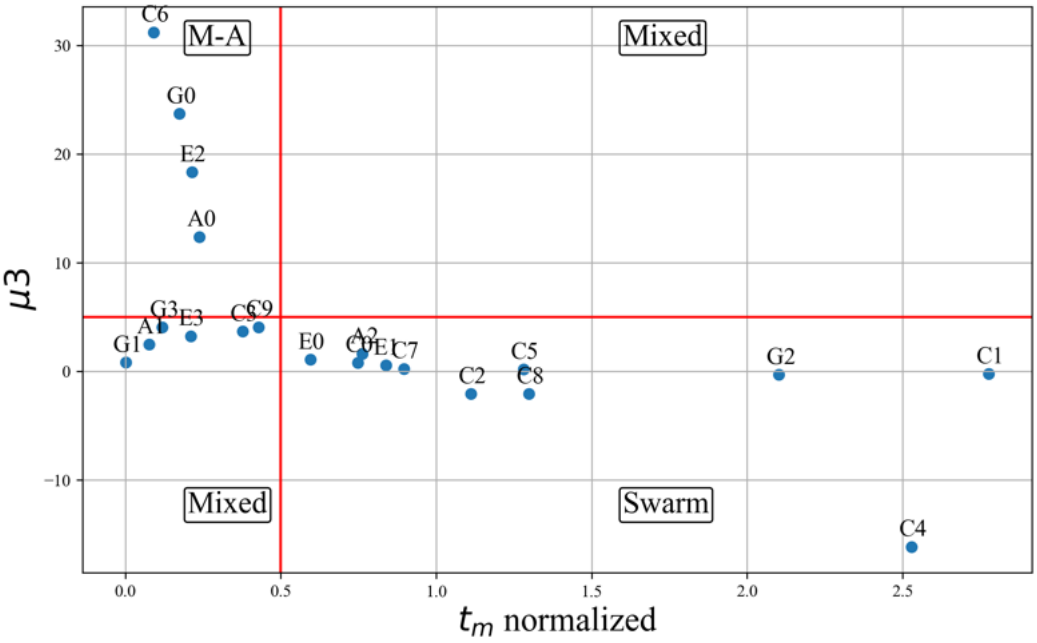

Figure 5 Cluster classification following the approach of Zhang and Shearer (2016). The plot shows the normalized timing of the largest event (t_m) relative to the mean, plotted against the skewness ($\mu 3$) of the moment release over time, calculated as described by Roland and McGuire (2009). Red lines delineate the classification boundaries that distinguish mainshock–aftershock (M–A) sequences from swarm-like activity. Mixed clusters include various types of fore-mainshock (F–M) patterns, as defined by Peng and Lei (2025).

the front slows down over time. The Cittareale sequence is characterized by migration velocities comparable to those observed in clusters from 2010 to 2016 (0.2–0.3 km/day, see Fig. S8), which are characterized by fewer earthquakes, reduced spatial extent, and occasional small burst-like sequences with varying magnitudes.

Figures 7c and 7d show clusters E1 and E2, which preceded the four $M_W > 5$ events of 18 January 2017, and were activated 1–2 days after the M_W 6.5 Norcia earthquake (30 October, 2016). Cluster E1 initially released low-magnitude events at 10–12 km depth along a 3 km long fault patch. We also observe a simultaneous initial activation of low-magnitude events along 3–4 km long segments for cluster E2, which occurs almost simultaneously with E1 but is shallower and located on a conjugate minor fault of the main Laga fault. This common phase is followed by a second stage characterized by an increase in the number of events (still of relatively low magnitude), with seismicity distributed across different compartments. During this phase, cluster E1 shows an increase in migration velocity, while cluster E2 maintains a more uniform migration rate. The spatial distribution of events in these clusters appears more complex and less clearly defined.

4.3 Diffusivity and effective stress drop

To better understand the physical mechanisms governing seismic cluster evolution, we estimate diffusivity and effective stress drop. These parameters provide insights into fluid migration and stress redistribution, which are critical for interpreting cluster dynamics and their triggering processes (Shapiro et al., 1997; Hainzl et al., 2012). Diffusivity reflects the efficiency of pore-pressure diffusion, often linked to fluid-driven seismicity, while effective stress drop constrains the energy release and fault strength during rupture (Abercrombie, 1995). Together, these estimates help assess whether clusters are controlled by fluid flow, stress transfer, or a combination of both.

The diffusivity values (D) of the triggering seismic front, calculated using the Shapiro formula (e.g., Shapiro and Dinske, 2009), are estimated for the clusters shown in Figure 7. These values are presented in Figure 8 for clusters A1, A2, E1, and E2, and in Figure S7 for several smaller swarms identified during the 2010–2016 phase. Clusters A1 and E1 initially display lower diffusivity values, which increase approximately two days after the onset of self-sustained slip propagation. In contrast, clusters A2 (Cittareale) and E2, located at shallower depths, exhibit different geometrical characteristics and consistently lower diffusivity values. Values of D around 30 m^2/s are observed for cluster A1 (Fig. 8a), where an initial phase of lower diffusivity, approximately 10 m^2/s during the first two days after the L'Aquila mainshock, is followed by sustained acceleration and widespread propagation of seismic events towards the northwest. At a similar depth, although with a more complex evolution and lower diffusivity, cluster E1 shows a comparable pattern with an increase in diffusivity about two days after the onset (Fig. 8c). In contrast, clusters A2 (Cittareale) and E2 display complex

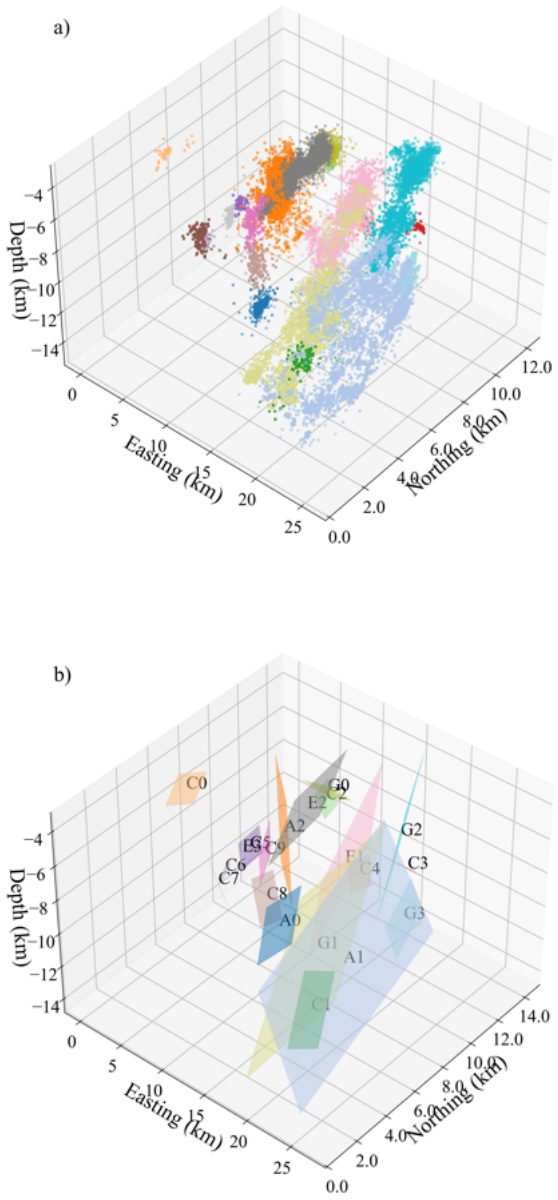

Figure 6 a) Three-dimensional visualization of seismic clusters, each represented with a distinct color to highlight spatial separation. b) Cluster geometries approximated by 3D planes derived from PCA analysis. The supplementary Movie M3 provides an interactive view to better illustrate the dominant orientations and spatial relationships among the clusters.

behavior, where pore pressure and diffusivity values of the seismic front decrease over time. In Figure S6, we also present examples of smaller clusters, located at the edges of the fault system and at shallower depth, for which D remains below 1–2 m^2/s.

Cluster A1 can be used to estimate the decrease in strength of the Laga fault after the main L'Aquila earthquake in 2009 due to pore fluid pressure. We determined the normal and shear stresses on the fault using formulas derived in Malagnini et al. (2010, 2012) and fault parameters given in Table 3. Details are provided in supplementary material. The result in Figure 9 shows that the effective strength of the fault decreases by about 0.5-1 MPa after 2 days to about 4.5-8 MPa after 5 days, which may explain the migration of events and the occurrence of the two subsequent M>5 events in the CSZ.

Parameter	Values
Average Fault Dip	40 degrees
Diffusivity	30 m^2/s
Static Friction (μ_S)	0.65–0.75–0.85
Fluid Density	1000 kg/m^3
Rock Density	3000 kg/m^3
Reference Depth	8000 m
Pore Pressure Coefficient (λ)	0.7–0.8–0.9
Distance from the origin point	7800 m
System condition	steady state
State (dry or wet)	wet
Fault type	normal

Table 3 Reference parameters used to estimate the decrease of fault strength as in Malagnini et al. (2010).

As shown in Figure 6, the area of each cluster can be estimated using the convex hull algorithm to define polyhedra enclosing the events belonging to the cluster, and the cumulative seismic moment can be estimated according to the relationships of Malagnini and Munafò (2018). The effective stress drop is calculated assuming that all the events are in a plane and using the formulas of Fischer and Hainzl (2017). From the total area we calculated the equivalent radius of the cluster, and then by summing the seismic moment of the events in the cluster, it is possible to determine the effective stress-drop. Figure 10 shows that the area occupied by clusters A1, G1 and G2 appear oversized in relation to the cumulative moment. This may indicate an aseismic contribution during the activation of the multiple $M_W > 5$ events. Relatively low effective stress drops (approximately 0.1 MPa) are also observed in the clusters preceding the series of four $M_W > 5$ events on 18 January 2017 (E1, E2). This is generally not the case for the clusters from 2010 to 2016, which have an average effective stress drop between 0.1 and 1 MPa.

In the CSZ, the estimated low effective stress drop can be related to the reported deficit between seismic and geodetic moment release after the 2009 and 2016 sequences (e.g., Gualandi et al., 2014; Cheloni et al., 2019; Mandler et al., 2021). A similar deficit of approximately 35% between seismic and geodetic cumulative moment is found by Vičič et al. (2020) in the finite fault inversions in the same area.

5 Discussion

High-resolution seismic catalogs enable detailed reconstructions of earthquake patterns, which are essential for understanding the evolution of clusters within complex fault systems. In these volumes, diverse fault segments interact through mechanisms ranging from fault creep to stick-slip behavior, influenced by internal forces and the three dimensional geometry of the fault network (e.g., Lee et al., 2024). Lithological het-

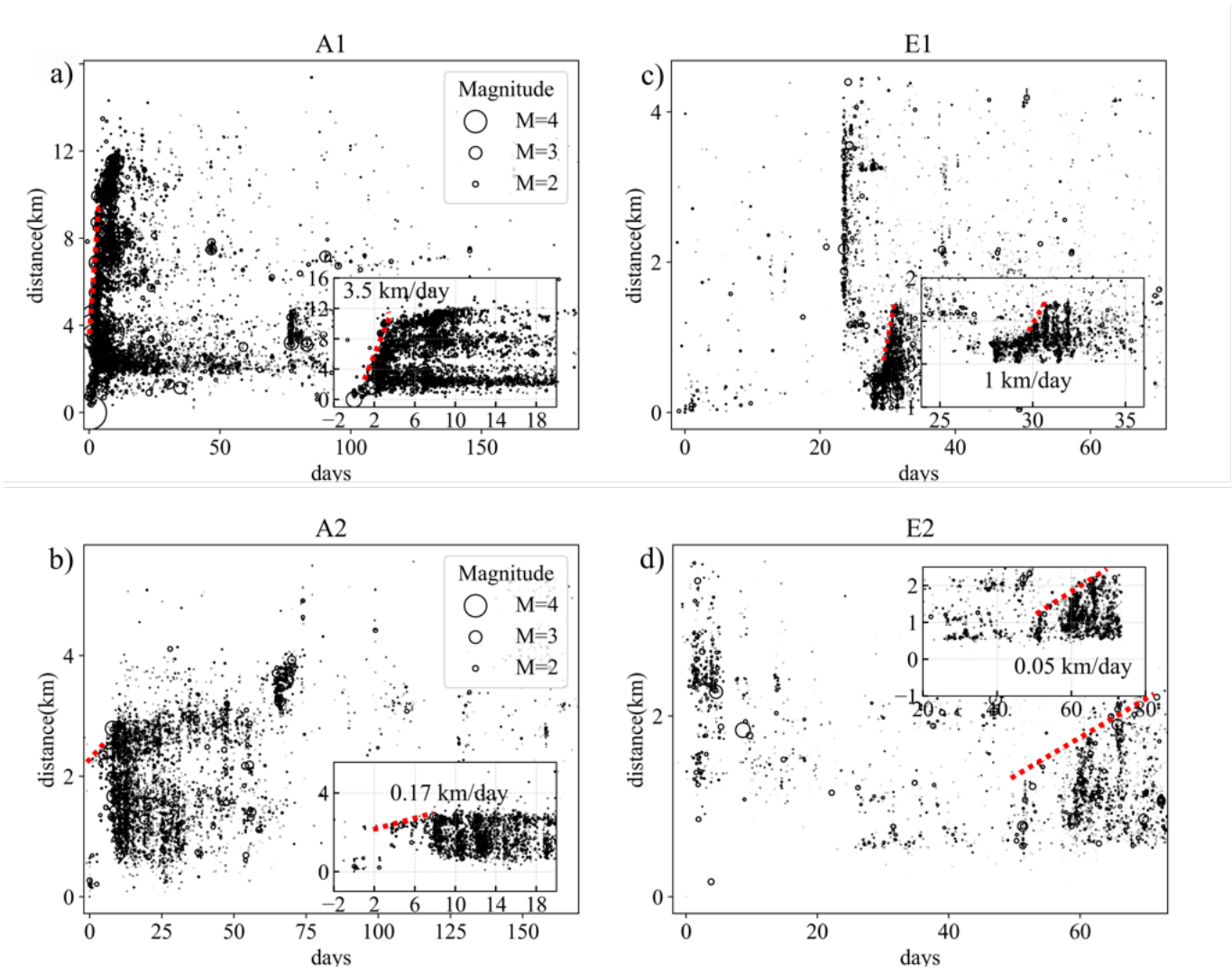

Figure 7 Migration velocity of the seismicity front for clusters (a) A1, (b) A2, (c) E1, and (d) E2. Red dotted lines represent the maximum migration velocity within each cluster. Insets provide zoomed-in views of selected time intervals to illustrate short-term variations and fluctuations in migration dynamics.

erogeneities and structural complexities play a critical role in fault behavior: they influence fault segmentation and bending, modulate the spatial distribution of stress, and the dynamics of rupture propagation. Tectonically driven sequences—such as those governed by aseismic slip or regional strain can facilitate stress transfer across fault segments, promoting rupture jumping (Roche et al., 2025). This process is more efficient when fault orientation and elevated pore pressure favor connectivity. In contrast, fluid-driven sequences typically exhibit slower migration rates and limited stress transfer, often manifesting as swarm-like seismicity in fractured, low-permeability volumes (Moutote et al., 2023; Roche et al., 2025). Static stress changes from prior earthquakes further influence the timing (advancing or delaying; Perfettini et al., 2003) and magnitude of subsequent ruptures (Pino et al., 2019).

The Laga fault in CSZ exemplifies the complexity of normal fault systems. Its geometry is non-planar, with dip angles varying from 50° to 30° along strike and with depth, as evidenced by seismic data (Bigi et al., 2013), geomorphological data (Faure Walker et al., 2021), focal mechanisms (Locchi et al., 2024), cluster-fitting planes (Fig. 6), and the nucleation of larger events, which generally occurs at changes in fault dip angle (Chiaraluce et al., 2011).

Such geometric variability induces a heterogeneous stress field that modulates slip behavior. Similar segmentation and bending were observed during the 1997 Colfiorito sequence, where six M_W 5–6 events ruptured distinct fault segments due to interactions between active normal faults and inherited thrust structures (Chiaraluce et al., 2003).

The lithological architecture of the CSZ, dominated by alternating carbonate platforms, flysch sequences, and marly units, plays a pivotal role in modulating fault permeability and seismic behavior. High-permeability fractured carbonates facilitate fluid migration and pore pressure buildup, promoting aseismic slip and rapid migration in clustered seismicity. The low effective stress drop, most evident in clusters with a higher number of events and greater energy release, suggests a significant aseismic contribution. This interpretation aligns with the observed deficit between cumulative seismic moment and geodetic moment in CSZ (e.g., Mandler et al., 2021). In contrast, low-permeability

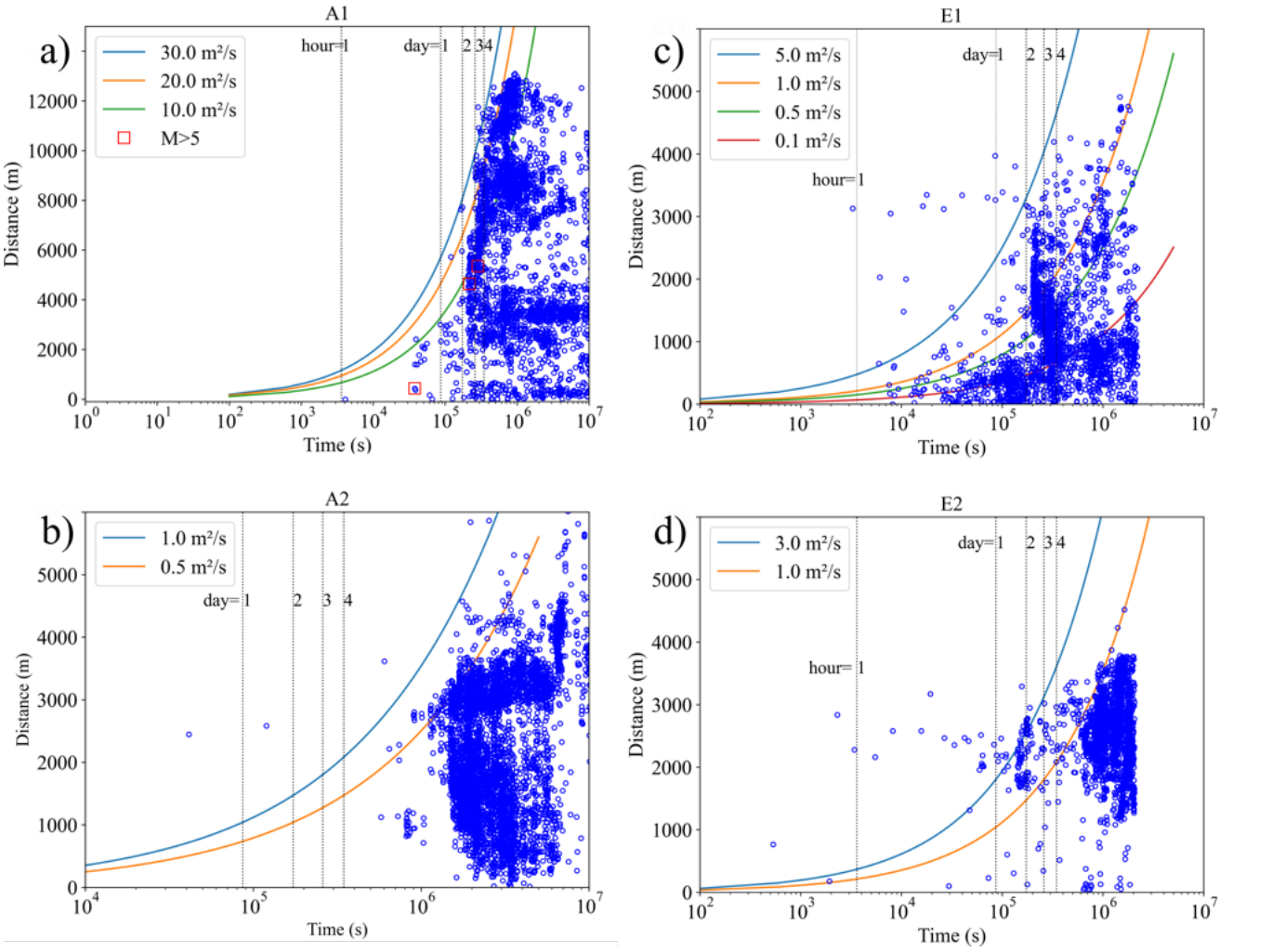

Figure 8 Diffusivity of the seismic front for clusters (a) A1, (b) A2, (c) E1, and (d) E2. Each panel displays the temporal evolution of diffusivity, highlighting distinct propagation behaviors across clusters. Clusters A1 and E1 initially display lower diffusivity values, which increase approximately two days after the onset of self-sustained slip propagation. In contrast, clusters A2 (Cittareale) and E2, located at shallower depths, show different geometrical characteristics and consistently lower diffusivity values.

flysch and marls compartmentalize the crust, leading to localized overpressure and swarm-like seismicity (e.g., Piana Agostinetti et al., 2017; Falcucci et al., 2018). These lithological contrasts, especially when juxtaposed across fault zones, create hydraulic discontinuities that influence the spatial distribution and migration of seismic clusters. Structural interpretations of the Campotosto linkage fault zone further suggest that lithological heterogeneity contributes to fault segmentation and influences rupture propagation (Tondi et al., 2020).

The CSZ experienced two major seismic sequences in 2009 and 2016–2017, within a confined area of approximately 450 km^2. These sequences were characterized by distinct activation mechanisms. In 2009, the segment of the Laga fault aligned with the Paganica fault—the source of the M_W 6.3 L'Aquila earthquake—was rapidly activated (Fig. 3a). Migration velocities of larger events increased from 1–2 km/day to 3–4 km/day within two days after the mainshock (Fig. 7a, cluster A1), likely driven by overpressurized fluids. A modeled fault strength reduction of 0.5–1 MPa at around 8 km depth (Fig. 9) is consistent with the low stress drop observed (Fig. 10), suggesting fluid channeling through permeable carbonate layers between 7 and 9 km depth.

In 2016, following the Amatrice earthquake, sparse seismicity appeared in the northern CSZ, but productive clusters (E1, E2) developed only after the Norcia event in late October (Movie M2). These clusters migrated northward and upward, in contrast to the prevailing southward background seismicity (Fig. 3e). Their migration followed the SE–NW rupture direction of all M_W > 5 events in the CSZ (Calderoni and Abercrombie, 2023), suggesting that cluster evolution may have weakened resistant fault segments, facilitating rupture. The northern CSZ, where flysch and marly units dominate (Barchi et al., 2021), exhibited slower cluster evolution and delayed rupture, consistent with fluid-influenced swarm behavior in low-permeability lithologies.

This preparatory phase lasted approximately 2.5 months and culminated in a cascade of four M_W >

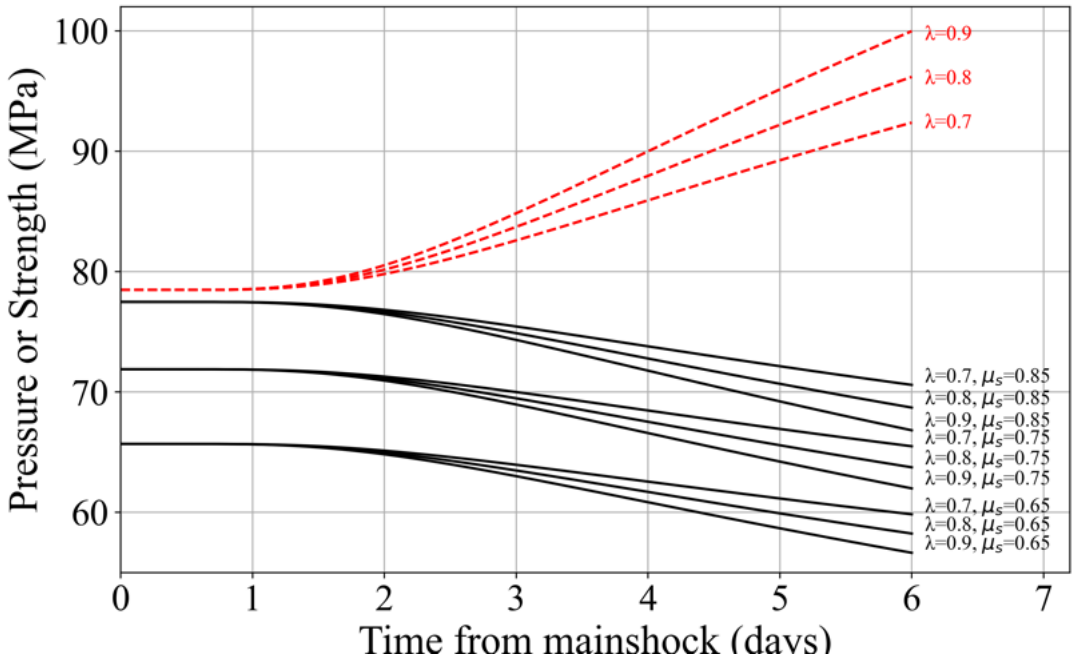

Figure 9 Temporal evolution of pore fluid pressure and effective fault strength following the mainshock (defined as the first event with $M_W > 5$ in the Campotosto sequence, occurring ~20 hours after the L'Aquila M_W 6.3 earthquake). Red dashed lines indicate the modeled pore fluid pressure. Simulations explore a range of static friction coefficients ($\mu_s = 0.65$–0.85) and initial pore fluid pressure ratios ($\lambda = 0.7$–0.9). The fault strength (black) decreases progressively, with a reduction of approximately 0.5–1 MPa after 2 days, and 4.5–8 MPa after 5 days, suggesting sustained weakening of the fault zone over time.

5 earthquakes on 18 January 2017 (Movie M2). During the interseismic period (2009–2016), low-magnitude clusters ($M_W < 3$) were scattered near the edges of the fault system (Fig. 4c). Some clusters aligned with tectonic features, while others—typically $M_W<2$—resembled fluid-induced swarms with multiphase bursts.

The contrasting triggering mechanisms of the strongest CSZ earthquakes and the evolution of clusters from 2009 to 2017 indicate a multiphase process. The 2009 sequence partially activated the Laga fault, assisted by high-pressure fluids and aseismic slip, with seismicity concentrated at depths of 7–9 km. Migration stopped at the subparallel Capitignano fault (Fig. 2), but shallow propagation resumed months later, likely due to fluid bypass, triggering the Cittareale sequence (cluster A2, Fig. 4a). This SE–NW migration followed the main tectonic alignments in the southern CSZ.

From 2010 to mid-2016, only minor clusters occurred near Cittareale, with low-rate seismicity prevailing. After the Amatrice earthquake, the northern CSZ was perturbed, and post-Norcia clusters formed on the Capitignano and Laga faults (E1, E2 in Fig. 5c), unlocking previously resistant fault sections. These ruptures propagated rapidly in January 2017, affecting both shallow and deep fault segments.

In summary, the interplay between fault geometry, segmentation, and lithological heterogeneity—particularly the distribution of permeable carbonates versus low-permeability flysch and marls—critically shaped the spatiotemporal evolution of seismicity in the CSZ. These factors likely inhibited a through-going $M_W > 6$ rupture along the Laga fault, underscoring the importance of integrating these data into seismic hazard assessments.

6 Conclusions

The Campotosto area has experienced several earthquakes with magnitudes in the range $5<M_W<5.5$, as well as sustained high-rate and long-lasting seismic activity in response to the perturbation generated by two large sequences that occurred nearby (within 30 km) in 2009 and 2016–2017. We analyzed clusters of seismicity and swarms that developed along the fault system to understand the interplay of processes that may have shaped the modality and patterns of seismicity over time in a region connecting the two volumes hosting the main faults responsible for the 2009 and 2016–17 mainshocks.

Our study shows that the migration of the seismic fronts in clusters and swarms exhibits a complex behavior characterized by alternating phases of accelerated expansion and slow, pressure-controlled diffusion. The duration of these clusters also varies considerably, ranging from a few days to several months, with migration velocities from kilometers to meters per day. This intricate pattern suggests a dynamic interplay between diffusion processes, and both aseismic and seismic slip across different fault segments. The effective stress drop within these clusters and swarms is estimated to be less than 1 MPa, indicating significant dif-

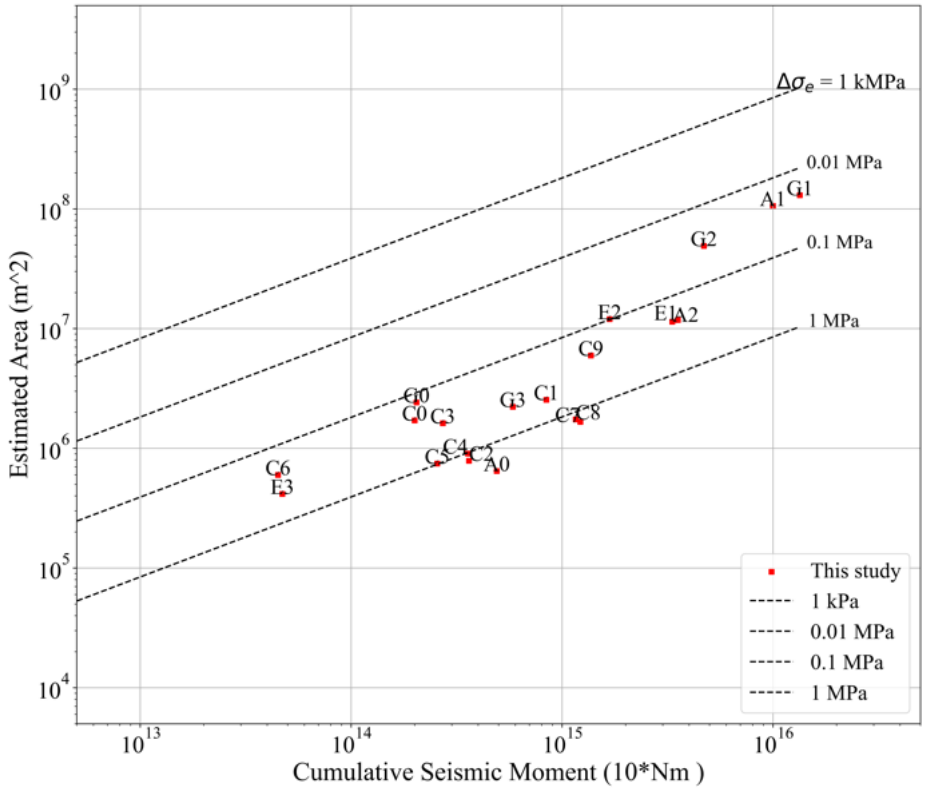

Figure 10 Cumulative seismic moment plotted against estimated rupture area for the clusters listed in Table 2. Most clusters align with an effective stress drop of approximately 0.1 MPa. Clusters with the largest estimated areas—such as G1, G2 and A1, which also exhibit the highest cumulative seismic moments—correspond to lower stress drop values (∼0.01 MPa). In contrast, clusters E1 and E2, which preceded the M > 5 events of January 18, 2017, show stress drop values close to 0.1 MPa. Smaller clusters display a broader range of stress drop estimates, spanning from 0.1 to 1 MPa.

ferences in stress release mechanisms. In particular, the lowest effective stress drop observed in widespread clusters suggests a substantial contribution from aseismic slip. This finding is consistent with geodetic studies that report a seismic moment deficit (30–35%) relative to the deformed area of the main events.

Our cluster analysis also indicates that the multiphase slip observed on the main fault in this area, the Laga fault, results from the combined effects of permeating fluids, complex geometry and lithological heterogeneities. Variations in the fault orientation and dip, both at shallow depths and below 10 km, as highlighted by the clusters, can create localized areas of higher and lower slip. This heterogeneity in slip distribution and fault segmentation can significantly influence the overall seismic moment and rupture propagation.

The 2017 seismic reactivation appears to have affected a broader portion of the fault system, with seismicity distributed across both deep and shallow fault segments. In contrast, the 2009 main events activated only a central part of the fault system, where fluids were channeled. This pattern may indicate a more complex rupture process and a change in the mechanical behavior of the fault, possibly influenced by fluid migration or evolving stress conditions. Analysing seismicity patterns and clusters triggered by transient processes is extremely valuable for understanding the faulting style of tectonic structures, as reflected in the spatio-temporal evolution of seismicity.

Acknowledgements

We thank the local and scientific committees of the International Workshop on Swarm-like Seismicity held in Castrovillari in October 2024, where a preliminary version of this work was presented before being further refined (http://www.swarmlikeseismicity.it). We also thank two anonymous referees and the editor Giuseppe Petrillo who helped to improve the paper by providing valuable comments and suggestions.

Data and code availability

The data to support this article are available via the European Integrated Data Archive managed by Istituto Nazionale di Geofisica e Vulcanologia (INGV, http://eida.rm.ingv.it/ Danecek et al., 2021).

The earthquake catalogs are: Valoroso et al. (2013) available at the repository (https://zenodo.org/records/4036248), Sugan et al. (2023) at (https://zenodo.org/

records/7515062), and Waldhauser et al. (2021) at (https://zenodo.org/records/5091137). TDMT focal mechanisms Locchi et al. (2024) are available at the repository (https://zenodo.org/records/10801577). HDBSCAN is available at (https://scikit-learn.org/). Scikit-learn libraries version 1.7.2. Computations are performed at CINECA in the framework of the HPC-TRES program agreement between OGS and CINECA.

Competing interests

The authors have no competing interests.

References

Abercrombie, R. E. Earthquake source scaling relationships from -1 to 5 ML using seismograms recorded at 2.5 km depth. *Journal of Geophysical Research: Solid Earth*, 100(B12):24015–24036, December 1995. doi: 10.1029/95JB02397.

Artale Harris, P., Scognamiglio, L., Magnoni, F., Casarotti, E., and Tinti, E. Centroid moment tensor catalog with 3D lithospheric wave speed model: The 2016–2017 Central Apennines sequence. *Journal of Geophysical Research: Solid Earth*, 127:e2021JB023068, December 2022. doi: 10.1029/2021JB023068.

Barchi, M. R., Carboni, F., Michele, M., Ercoli, M., Giorgetti, C., Porreca, M., et al. The influence of subsurface geology on the distribution of earthquakes during the 2016–2017 Central Italy seismic sequence. *Tectonophysics*, 807:228797, November 2021. doi: 10.1016/j.tecto.2021.228797.

Bigi, S., Casero, P., Chiarabba, C., and Di Bucci, D. Contrasting surface active faults and deep seismogenic sources unveiled by the 2009 L'Aquila earthquake sequence (Italy). *Terra Nova*, 25(1): 21–29, 2013. doi: 10.1111/ter.12000.

Bradford Barber, C., Dobkin, D. P., and Huhdanpaa, H. The Quickhull algorithm for convex hulls. *ACM Trans. Math. Softw.*, 22(4): 469–483, December 1996. doi: 10.1145/235815.235821.

Brennan Brunsvik, G., Morra, G., Cambiotti, G., Chiaraluce, L., Di Stefano, R., De Gori, P., and Yuen, D. A. Three-dimensional Paganica fault morphology obtained from hypocenter clustering (L'Aquila 2009 seismic sequence, Central Italy). *Tectonophysics*, 804, October 2021. doi: 10.1016/j.tecto.2021.228756.

Buttinelli, M., Petracchini, L., Maesano, F., D'Ambrogi, C., Scrocca, D., Marino, M., Capotorti, F., Bigi, S., Cavinato, G., Mariucci, M., Montone, P., and Di Bucci, D. The impact of structural complexity, fault segmentation, and reactivation on seismotectonics: Constraints from the upper crust of the 2016–2017 Central Italy seismic sequence area. *Tectonophysics*, 810, 2021. doi: 10.1016/j.tecto.2021.228861.

Calderoni, G. and Abercrombie, R. Investigating spectral estimates of stress drop for small to moderate earthquakes with heterogeneous slip distribution: Examples from the 2016–2017 Amatrice earthquake sequence. *Journal of Geophysical Research*, 128(6), June 2023. doi: 10.1029/2022jb025022.

Calderoni, G., Rovelli, A., and Di Giovambattista, R. Rupture directivity of the strongest 2016–2017 central Italy earthquakes. *Journal of Geophysical Research: Solid Earth*, 122:9118–9131, September 2017. doi: 10.1002/2017JB014118.

Campello, R. J. G. B., Moulavi, D., and Sander, J. Density-based clustering based on hierarchical density estimates. In *Pacific-Asia Conference on Knowledge Discovery and Data Mining . Springer*, pages 160–172. Springer, May 2013. doi: 10.1007/978-3-642-37456-2_14.

Campello, R. J. G. B., Moulavi, D., Zimek, A., and Sander, J. Hierarchical density estimates for data clustering, visualization, and outlier detection. *ACM Transactions on Knowledge Discovery from Data (TKDD)*, 10(1):1–51, January 2015. doi: 10.1145/2733381.

Carpenter, B. M., Scuderi, M. M., Collettini, C., and Marone, C. Frictional heterogeneities on carbonate-bearing normal faults: Insights from the Monte Maggio Fault, Italy. *Journal of Geophysical Research: Solid Earth*, 119, November 2014. doi: 10.1002/2014JB011337.

Cheloni, D., D'Agostino, N., Scognamiglio, L., et al. Heterogeneous behavior of the Campotosto normal fault (Central Italy) imaged by InSAR GPS and strong-motion data: Insights from the 18 January 2017 events. *Remote Sensing*, 11(12):1482, June 2019. doi: 10.3390/rs11121482.

Chiarabba, C., De Gori, P., Cattaneo, M., et al. Faults geometry and the role of fluids in the 2016–2017 Central Italy seismic sequence. *Geophysical Research Letters*, 45(14):6963–6971, July 2018. doi: 10.1029/2018gl077485.

Chiaraluce, L., Ellsworth, W. L., Chiarabba, C., and Cocco, M. Imaging the complexity of an active normal fault system: The 1997 Colfiorito (central Italy) case study. *Journal of Geophysical Research*, 108(B6):2294, June 2003. doi: 10.1029/2002JB002166.

Chiaraluce, L., Valoroso, L., Piccinini, D., Di Stefano, R., and De Gori, P. The anatomy of the 2009 L'Aquila normal fault system (central Italy) imaged by high resolution foreshock and aftershock locations. *Journal of Geophysical Research: Solid Earth*, 116(B12), 2011. doi: 10.1029/2011JB008352.

Chiaraluce, L., Di Stefano, R., Tinti, E., Scognamiglio, L., Michele, M., Casarotti, E., Cattaneo, M., De Gori, P., Chiarabba, C., Monachesi, G., Lombardi, A., Valoroso, L., Latorre, D., and Marzorati, S. T. Central Italy Seismic Sequence: A First Look at the Mainshocks, Aftershocks, and Source Models. *Seismological Research Letters*, 88(3):757–771, March 2017. doi: 10.1785/0220160221.

Chiaraluce, L., Michele, M., Waldhauser, F., et al. A comprehensive suite of earthquake catalogues for the 2016–2017 Central Italy seismic sequence. *Scientific Data*, 9(1), January 2022. doi: 10.1038/s41597-022-01827-z.

Cirella, A., Piatanesi, A., Cocco, M., Tinti, E., Scognamiglio, L., Michelini, A., Lomax, A., and Boschi, E. Rupture history of the 2009 L'Aquila (Italy) earthquake from non-linear joint inversion of strong motion and GPS data. *Geophysical Research Letters*, 36:L19304, October 2009. doi: 10.1029/2009GL039795.

Civico, R., Blumetti, A. M., Chiarini, E., Cinti, F. R., La Posta, E., Papasodaro, F., Sapia, V., Baldo, M., Lollino, G., and Pantosti, D. Traces of the active Capitignano and San Giovanni faults (Abruzzi Apennines, Italy). *Journal of Maps*, 12(sup1):453–459, October 2016. doi: 10.1080/17445647.2016.1239229.

Collettini, C. and Tinti, E. The influence of lithology and fault source volume on the magnitude–frequency distribution of earthquakes. *Geophysical Research Letters*, 52, January 2025. doi: 10.1029/2024GL110354.

Danecek, P., Pintore, S., Mazza, S., Mandiello, A., Fares, M., Carluccio, I., Della Bina, E., Franceschi, D., Moretti, M., Lauciani, V., Quintiliani, M., and Michelini, A. The Italian Node of the European Integrated Data Archive. *Seismological Research Letters*, 92(3):1726–1737, 03 2021. doi: 10.1785/0220200409.

De Gori, P., Michele, M., Chiaraluce, L., and Chiarabba, C. Fault rheology control on rupture propagation and aftershocks distribution during the 2016–2017 Central Italy earthquakes. *Seismological Research Letters*, 94(6):2642–2654, December 2023. doi: 10.1785/0220220284.

Essing, D. and Poli, P. Unraveling earthquake clusters compos-

ing the 2014 Alto Tiberina earthquake swarm via unsupervised learning. *Journal of Geophysical Research: Solid Earth*, February 2024. doi: 10.1029/2022JB026237.

Ester, M., Kriegel, H.-P., Sander, J., and Xu, X. A density-based algorithm for discovering clusters in large spatial databases with noise. In *Proceedings of the Second International Conference on Knowledge Discovery and Data Mining*, pages 226–231, August 1996. doi: 10.5555/3001460.3001507.

Falcucci, E., Gori, S., Bignami, C., Pietrantonio, G., Melini, D., Moro, M., Saroli, M., and Galadini, F. The Campotosto seismic gap in between the 2009 and 2016–2017 seismic sequences of central Italy and the role of inherited lithospheric faults in regional seismotectonic settings. *Tectonics*, 37:2425–2445, November 2018. doi: 10.1029/2017TC004844.

Faure Walker, J. P., Boncio, P. B., Roberts, G. P., Benedetti, L., Scotti, O., Visini, F., and Peruzza, L. Fault2SHA Central Apennines database and structuring active fault data for seismic hazard assessment. *Scientific Data*, 8(1):87, March 2021. doi: 10.1038/s41597-021-00868-0.

Fischer, T. and Hainzl, S. Effective Stress Drop of Earthquake Clusters. *Bulletin of the Seismological Society of America*, 107(5): 2247–2257, 09 2017. doi: 10.1785/0120170035.

Fischer, T. and Hainzl, S. The Growth of Earthquake Clusters. *Frontiers in Earth Science*, 9, April 2021. doi: 10.3389/feart.2021.638336.

Gualandi, A., Serpelloni, E., and Belardinelli, M. E. Space–time evolution of crustal deformation related to the Mw 6.3, 2009 L'Aquila earthquake (central Italy) from principal component analysis inversion of GPS position time-series. *Geophysical Journal International*, 197(1):174–191, January 2014. doi: 10.1093/gji/ggt522.

Hainzl, S. Seismicity patterns of earthquake swarms due to fluid intrusion and stress triggering. *Geophysical Journal International*, 159(3):1090–1096, December 2004. doi: 10.1111/j.1365-246X.2004.02463.x.

Hainzl, S., Fischer, T., and Dahm, T. Seismicity-based estimation of the driving fluid pressure in the case of swarm activity in Western Bohemia. *Geophysical Journal International*, 191(1): 271–281, October 2012. doi: 10.1111/j.1365-246X.2012.05610.x.

Hunt, E. L. and Reffert, S. Improving the open cluster census. *Astronomy and Astrophysics*, 646:A104, February 2021. doi: 10.1051/0004-6361/202039341.

Lavecchia, G., Bello, S., Andrenacci, C., Cirillo, D., Ferrarini, F., Vicentini, N., de Nardis, R., and Brozzetti, F. *QUaternary fault strain INdicators database: QUIN 1.0 - first release from the Apennines of central Italy*. PANGAEA, 2021. doi: 10.1594/PANGAEA.934802.

Lee, J., Tsai, V. C., Chatterjee, A., and Trugman, D. T. Fault-network geometry influences earthquake frictional behaviour. *Nature*, 631(106):110, July 2024. doi: 10.1038/s41586-024-07518-6.

Lelis, L. and Sander, J. Semi-supervised density-based clustering. In *IEEE 9th International Conference on Data Mining*, pages 842–847, November 2009. doi: 10.1109/ICDM.2009.143.

Locchi, M. E., Scognamiglio, L., Tinti, E., and Collettini, C. A large fault partially reactivated during two contiguous seismic sequences in Central Italy: The role of geometrical and frictional heterogeneities. *Tectonophysics*, 877:230284, February 2024. doi: 10.1016/j.tecto.2024.230284.

Lomax, A., Virieux, J., Volant, P., and Berge-Thierry, C. Probabilistic earthquake location in 3D and layered models. In Thurber, C. H. and Rabinowitz, N., editors, *Advances in Seismic Event Location. Modern Approaches in Geophysics, 18*. Springer, Dordrecht, 2000. doi: 10.1007/978-94-015-9536-0_5.

Magnoni, F., Casarotti, E., Komatitsch, D., et al. Adjoint tomography of the Italian lithosphere. *Communications Earth and Environment*, 3:69, April 2022. doi: 10.1038/s43247-022-00397-7.

Malagnini, L. and Munafò, I. On the Relationship between MwMw and M0M0 in a Broad Range: An Example from the Apennines, Italy. *Bulletin of the Seismological Society of America*, 108(2): 1018–1024, February 2018. doi: 10.1785/0120170303.

Malagnini, L., Nielsen, S., Mayeda, K., and Boschi, E. Energy radiation from intermediate- to large-magnitude earthquakes: Implications for dynamic fault weakening. *Journal of Geophysical Research*, 115:B06319, June 2010. doi: 10.1029/2009JB006786.

Malagnini, L., Lucente, F. P., De Gori, P., Akinci, A., and Munafo', I. Control of pore fluid pressure diffusion on fault failure mode: Insights from the 2009 L'Aquila seismic sequence. *Journal of Geophysical Research*, 117:B05302, May 2012. doi: 10.1029/2011JB008911.

Mancini, S., Segou, M., Werner, M. J., Parsons, T., Beroza, G., and Chiaraluce, L. On the use of high-resolution and deep-learning seismic catalogs for short-term earthquake forecasts: Potential benefits and current limitations. *Journal of Geophysical Research: Solid Earth*, 127, e2022JB025202, November 2022. doi: 10.1029/2022JB025202.

Mandler, E., Pintori, F., Gualandi, A., Anderlini, L., Serpelloni, E., and Belardinelli, M. E. Post-seismic deformation related to the 2016 Central Italy seismic sequence from GPS displacement time-series. *Journal of Geophysical Research: Solid Earth*, 126, e2021JB022200, September 2021. doi: 10.1029/2021JB022200.

Moratto, L., Santulin, M., Tamaro, A., et al. Near-source ground motion estimation for assessing the seismic hazard of critical facilities in central Italy. *Bulletin of Earthquake Engineering*, 21: 53–75, January 2023. doi: 10.1007/s10518-022-01555-0.

Moutote, L., Itoh, Y., Lengliné, O., Duputel, Z., and Socquet, A. Evidence of a transient aseismic slip driving the 2017 Valparaiso earthquake sequence, from foreshocks to aftershocks. *Journal of Geophysical Research: Solid Earth*, 128: e2023JB026603, March 2023. doi: 10.1029/2023JB026603.

Peng, Z. and Lei, X. Physical mechanisms of earthquake nucleation and foreshocks: Cascade triggering, aseismic slip, or fluid flows? *Earthquake Research Advances*, 5(2):100349, 2025. doi: 10.1016/j.eqrea.2024.100349.

Perfettini, H., Schmittbuhl, J., and Cochard, A. Shear and normal load perturbations on a two-dimensional continuous fault: 1. Static triggering. *Journal of Geophysical Research: Solid Earth*, 108(B9), 2003. doi: 10.1029/2002JB001804.

Piana Agostinetti, N., Giacomuzzi, G., and Chiarabba, C. Seismic swarms and diffuse fracturing within Triassic evaporites fed by deep degassing along the low-angle Alto Tiberina normal fault (central Apennines, Italy). *Journal of Geophysical Research: Solid Earth*, 122(1):308–331, 01 2017. doi: 10.1002/2016JB013295.

Piegari, E., Camanni, G., Mercurio, M., and Marzocchi, W. Illuminating the hierarchical segmentation of faults through an Unsupervised Learning Approach applied to clouds of earthquake hypocenters. *Earth and Space Science*, 11:e2023EA003267, February 2024. doi: 10.1029/2023EA003267.

Pino, N. A., Convertito, V., and Madariaga, R. Clock advance and magnitude limitation through fault interaction: The case of the 2016 central Italy earthquake sequence. *Scientific Reports*, 9(1): 5005–5005, March 2019. doi: 10.1038/s41598-019-41453-1.

Pizzi, A., Di Domenica, A., Galluzzo, F., and Innocenti, C. Fault segmentation as constraint to the occurrence of the main shocks of the 2016 Central Italy seismic sequence. *Tectonics*, 36(12), December 2017. doi: 10.1002/2017TC004652.

Roche, V., van der Baan, M., and Walsh, J. The role of the three-dimensional geometry of fault steps on event migration dur-

ing fluid-induced seismic sequences. *Journal of Geophysical Research: Solid Earth*, 130: e2024JB029476, April 2025. doi: 10.1029/2024JB029476.

Roland, E. and McGuire, J. J. Earthquake swarms on transform faults. *Geophysical Journal International*, 178(3):1677–1690, 2009. doi: 10.1111/j.1365-246X.2009.04214.x.

Rousseeuw, P. J. Silhouettes: a Graphical Aid to the Interpretation and Validation of Cluster Analysis. *Computational and Applied Mathematics*, 20:53–65, November 1987. doi: 10.1016/0377-0427(87)90125-7.

Schoenball, M. and Ellsworth, W. L. A systematic assessment of the spatiotemporal evolution of fault activation through induced seismicity in Oklahoma and Southern Kansas. *Journal of Geophysical Research: Solid Earth*, 122(12):10189–10206, June 2017. doi: 10.1002/2017JB014850.

Shapiro, S. A. and Dinske, C. Scaling of seismicity induced by nonlinear fluid-rock interaction. *Geophysical Research Letters*, 36: L18302, September 2009. doi: 10.1029/2009GL039500.

Shapiro, S. A., Huenges, E., and Borm, G. Estimating the crust permeability from fluid-injection-induced seismic emission at the KTB site. *Geophysical Journal International*, 131(2):15–18, November 1997. doi: 10.1111/j.1365-246X.1997.tb01215.x.

Soldati, G., Zaccarelli, L., and Faenza, L. Spatio-temporal seismic velocity variations associated to the 2016–2017 central Italy seismic sequence from noise cross-correlation. *Geophysical Journal International*, 219(3):2165–2173, September 2019. doi: 10.1093/gji/ggz429.

Spallarossa, D., Picozzi, M., Scafidi, D., Morasca, P., Turino, C., and Bindi, D. The RAMONES Service for Rapid Assessment of Seismic Moment and Radiated Energy in Central Italy: Concepts, Capabilities, and Future Perspectives. *Seismological Research Letters*, 92(3):1759–1772, May 2021. doi: 10.1785/0220200348.

Sugan, M., Kato, A., Miyake, H., Nakagawa, S., and Vuan, A. The preparatory phase of the 2009 Mw6.3 L'Aquila earthquake by improving the detection capability of low-magnitude foreshocks. *Geophysical Research Letters*, 41:6137–6144, September 2014. doi: 10.1002/2014GL061199.

Sugan, M., Campanella, S., Chiaraluce, L., Michele, M., and Vuan, A. The unlocking process leading to the 2016 Central Italy seismic sequence. *Geophysical Research Letters*, 50:e2022GL101838, August 2023. doi: 10.1029/2022GL101838.

Tan, Y. J., Waldhauser, F., Ellsworth, W. L., Zhang, M., Zhu, W., Michele, M., Chiaraluce, L., Beroza, G. C., and Segou, M. Machine-Learning-Based High-Resolution Earthquake Catalog Reveals How Complex Fault Structures Were Activated during the 2016–2017 Central Italy Sequence. *The Seismic Record*, 1(1): 11–19, January 2021. doi: 10.1785/0320210001.

Tinti, E., Scognamiglio, L., Michelini, A., and Cocco, M. Slip heterogeneity and directivity of the ML 6.0, 2016, Amatrice earthquake estimated with rapid finite-fault inversion. *Geophysical Research Letters*, 43(10):745–10, February 2016. doi: 10.1002/2016GL071263.

Tondi, E., Jablonska, D., Volatili, T., Michele, M., et al. The Campotosto linkage fault zone between the 2009 and 2016 seismic sequences of central Italy: Implications for seismic hazard analysis. *Geological Society of America Bulletin*, 133:1679–1694, March 2020. doi: 10.1130/b35788.1.

Valoroso, L., Chiaraluce, L., Piccinini, D., Di Stefano, R., Schaff, D., and Waldhauser, F. Radiography of a normal fault system by 64,000 high-precision earthquake locations: The 2009 L'Aquila (central Italy) case study. *Journal of Geophysical Research: Solid Earth*, 118:1156–1176, April 2013. doi: 10.1002/jgrb.50130.

Vičič, B., Aoudia, A., Borghi, A., Momeni, S., and Vuan, A. Seismicity rate changes and geodetic transients in Central Apennines. *Geophysical Research Letters*, 47:e2020GL090668, May 2020. doi: 10.1029/2020GL090668.

Vuan, A., Sugan, M., Chiaraluce, L., and Di Stefano, R. Loading rate variations along a midcrustal shear zone preceding the Mw6.0 earthquake of 24 August 2016 in Central Italy. *Geophysical Research Letters*, 44(12):170–12, June 2017. doi: 10.1002/2017GL076223.

Waldhauser, F. and Ellsworth, W. L. A double-difference earthquake location algorithm: Method and application to the northern Hayward fault. *Bull. Seism. Soc. Am.*, 90:1353–1368, December 2000. doi: 10.1785/0120000006.

Waldhauser, F., Michele, M., Chiaraluce, L., Di Stefano, R., and Schaff, D. P. Fault planes, fault zone structure and detachment fragmentation resolved with high-precision aftershock locations of the 2016–2017 Central Italy sequence. *Geophysical Research Letters*, 48(16), August 2021. doi: 10.1029/2021GL092918.

Ward, J. H. Hierarchical grouping to optimize an objective function. *Journal of the American Statistical Association*, 58(301):236–244, September 1963. doi: 10.1080/01621459.1963.10500845.

Zhang, Q. and Shearer, P. M. A new method to identify earthquake swarms applied to seismicity near the San Jacinto Fault, California. *Geophysical Journal International*, 205(2):995–1005, 02 2016. doi: 10.1093/gji/ggw073.